Research Square

Preprints are preliminary reports that have not undergone peer review.
They should not be considered conclusive, used to inform clinical practice,
or referenced by the media as validated information.

Multiparametric MRI Habitat Analysis for Preoperative Prediction of Tumor Budding and Prognosis in Rectal Adenocarcinoma

jing Zhang
Northwestern Polytechnical University
longchao Li
Shaanxi Provincial People's Hospital
min Tang
Shaanxi Provincial People's Hospital
xiaoyan Lei
Shaanxi Provincial People's Hospital
li Zhang
182029903550139.com

Shaanxi Provincial People's Hospital
xianglong Duan
Northwestern Polytechnical University

Research Article

Keywords: Rectal adenocarcinoma, Tumor budding, Amide proton transfer-weighted MRI, Multiparametric MRI, Tumor habitat, Radiomics, Preoperative prognosis

Posted Date: November 23rd, 2026

DOI: https://doi.org/10.21203/rs.3.rs-11366010/v1

License: This work is licensed under a Creative Commons Attribution 4.0 International License.
Read Full License

Additional Declarations: No competing interests reported.

Multiparametric MRI Habitat Analysis for Preoperative Prediction of Tumor Budding and Prognosis in Rectal Adenocarcinoma

Jing Zhang 1,2, Longchao Li2, Min Tang2, Xiaoyan Lei2, Li Zhang *2, Xianglong Duan* 1,3

*These authors contributed equally to this work.

[1] School of Life Science and Technology, Northwestern Polytechnical University, Xi'an 710072, China

[2] Department of Magnetic Resonance Imaging, Shaanxi Provincial People's Hospital, Xi'an 710068, China

[3] Second Department of General Surgery, Shaanxi Provincial People's Hospital, Xi'an 710068, China

Corresponding authors: Li Zhang, MD, PhD, Department of Magnetic Resonance Imaging, Shaanxi Provincial People's Hospital, No.256 Youyi Road, Xi'an, 710068, Shaanxi, China.

Tel.: +86-29-85251331-2704, **Fax**: +86-29-85236987, **E-mail:** 18202990355@139.com

Xianglong Duan, MD, PhD, School of Life Science and Technology, Northwestern Polytechnical University, Xi'an 710072, Shaanxi, China; Second Department of General Surgery, Shaanxi Provincial People's Hospital, No.256 Youyi Road, Xi'an 710068, Shaanxi, China.

Tel.: +86-29-85251331-2583, **Fax:** +86-29-85236987, **E-mail:** duanxianglong@nwpu.edu.cn

Abstract

Objective Tumour budding (TB) is an independent pathological-prognostic biomarker for rectal adenocarcinoma (RA) that guides therapy stratification. Conventional MRI and whole-tumor radiomics poorly capture intratumoral heterogeneity, which limits the preoperative prediction of TB grade. Amide proton transfer-weighted (APTw) MRI reflects endogenous tumour protein metabolism and provides additional value for evaluating tumour microenvironment heterogeneity. This study aimed to develop and validate a multiparametric MRI habitat-based radiomics model integrating APTw, DWI/ADC, and T2WI for preoperative prediction of high-grade TB and prognostic stratification in patients with RA.

Materials and methods A total of 157 pathologically confirmed RA patients who underwent preoperative 3.0 T multiparametric MRI including APTw were enrolled. Tumour habitats were segmented using superpixel partitioning and K-means clustering, and habitat-level radiomic features were screened to discriminate low-intermediate-grade TB (Bd 1+2) from high-grade TB (Bd 3). LASSO regression was applied for feature reduction, and logistic regression was used for model construction. Model performance was evaluated by ROC analysis with K-fold cross-validation. The DeLong test, calibration curves, and decision-curve analysis (DCA) were used for model comparison and net-benefit assessment. Kaplan-Meier survival analysis, the log-rank test, and Cox regression were performed for prognostic evaluation.

Results Habitat-based radiomics outperformed whole-tumor radiomics and the pure clinical model. The APTw+ADC habitat-based model achieved the optimal performance (AUC of 0.931), accompanied by favourable calibration and clinical net benefit. Patients predicted to have Bd 3 demonstrated significantly worse disease-free survival (DFS).

Conclusion Multiparametric MRI habitat-based radiomics can characterise intratumoral metabolic-structural heterogeneity in RA. The APTw+ADC habitat-based model allows accurate non-invasive preoperative prediction of high-grade TB and prognostic risk-stratification to support clinical decision-making.

Keywords Rectal adenocarcinoma; Tumor budding; Amide proton transfer-weighted MRI; Multiparametric MRI; Tumor habitat; Radiomics; Preoperative prognosis

Introduction

Colorectal cancer (CRC) ranks as the third most prevalent malignancy worldwide and contributes substantially to global cancer-related mortality, with distinct clinicopathological features and heterogeneous prognostic outcomes across patient subgroups. Rectal adenocarcinoma (RA) accounts for 30%–40% of all CRC cases and poses considerable clinical challenges, including rising incidence among younger populations and prominent intratumoral heterogeneity that complicates individualized treatment stratification [1–3]. The tumour-node-metastasis (TNM) staging system remains the mainstream clinical framework for treatment guidance and prognostic evaluation for RA. Nevertheless, conventional TNM staging relies primarily on macroscopic anatomical features and fails to fully reflect the intrinsic biological aggressiveness, invasive activity, and metastatic potential of individual tumours. Accumulating clinical evidence has demonstrated that 35%–40% of RA patients with identical TNM stages exhibit divergent therapeutic responses and long-term survival outcomes after standardized treatment [4,5]. This clinical discrepancy highlights the urgent need for reliable auxiliary prognostic biomarkers to refine risk stratification beyond traditional anatomical staging.

Tumour budding (TB) has been established as a robust pathological and prognostic biomarker for rectal cancer, closely correlated with malignant tumour phenotypes. Representing a morphological manifestation of epithelial-mesenchymal transition (EMT), TB reflects the detachment and invasive capacity of individual tumour cells from the primary lesion. High-grade TB is significantly associated with poor tumour differentiation, lymphovascular invasion, and lymph node metastasis, and serves as an independent adverse prognostic factor for overall and disease-free survival in RA patients [6,7]. Moreover, TB grade has been incorporated into routine rectal cancer clinical management. High-grade TB indicates a requirement for adjuvant chemotherapy for stage II RA and predicts unsatisfactory responses to neoadjuvant chemoradiation in locally advanced disease [8,9]. In addition, TB status acts as a critical reference index for determining supplementary radical surgery after endoscopic resection in early-stage rectal cancer [6]. Accordingly, accurate preoperative evaluation of TB grade is essential for optimizing risk stratification, prognostic assessment, and personalised treatment decision-making for RA patients [10,11].

Currently, pathological assessment of TB is predominantly performed on postoperative surgical specimens, which limits its value for preoperative clinical treatment planning. Preoperative endoscopic biopsy, the only available invasive sampling method for preoperative TB evaluation, is subject to inherent sampling bias. Preoperative endoscopic biopsy, the only available invasive sampling method for preoperative TB evaluation, is subject to inherent sampling bias. Owing to extensive intratumoral heterogeneity [13], small biopsy specimens cannot comprehensively represent the overall pathological characteristics of the entire tumour, resulting in inaccurate TB grading [12].Furthermore, invasive

biopsy may cause patient discomfort and carries potential procedural risks, limiting its widespread clinical application. Therefore, a non-invasive, comprehensive and accurate preoperative TB-grading method is urgently needed to improve preoperative risk evaluation for RA.

MRI-based radiomics and machine-learning techniques have shown promising potential for non-invasive preoperative prediction of TB grade in previous studies [14–17]. However, most existing studies adopt conventional whole-tumour feature-extraction strategies that average regional imaging signals, which cannot adequately capture spatially heterogeneous structural and metabolic alterations linked to aggressive tumour phenotypes. Tumour habitat imaging provides an innovative analytical paradigm for resolving intratumoral heterogeneity. Originating from ecological concepts, tumour habitats are biologically distinct intratumoral subregions with unique structural and functional properties [18]. Voxel-level habitat segmentation and quantitative analysis enable fine delineation of heterogeneous tumour subregions, allowing comprehensive characterisation of tumour microenvironmental heterogeneity at a microscopic imaging level [19].

Amide proton transfer-weighted (APTw) MRI is an advanced molecular imaging technique that provides endogenous subcellular protein metabolic information, offering complementary biological insights that cannot be obtained from conventional morphological and diffusion MRI sequences [20]. To date, only one preliminary study has attempted to predict TB grade using APTw MRI in RA; however, that study adopted conventional histogram analysis and failed to capture spatial tumour metabolic heterogeneity [21]. Furthermore, APTw has demonstrated predictive utility for tumour grading across multiple solid malignancies [22]. Against this background, the present study aimed to

construct and validate a novel multiparametric habitat radiomics model integrating APTw, diffusion-weighted imaging (DWI)/apparent diffusion coefficient (ADC), and T2-weighted imaging (T2WI), and to explore its clinical value in non-invasive preoperative TB-grade prediction and postoperative prognostic stratification for patients with RA.

Materials and methods

Patients

This prospective study was approved by the Ethics Review Committee of our hospital. Informed consent was obtained from all enrolled patients (approval number: 2022K-133).

From June 2022 to August 2024, we identified 418 consecutive RC patients who underwent surgical resection. The inclusion criteria were as follows: histopathologically confirmed RA diagnosis with TB grade assessment and preoperative MRI examination within 14 days prior to surgery. The exclusion criteria included the following: receipt of neoadjuvant therapy before resection; poor APTw-MRI quality or poorly visualized lesions; no surgery; special histological subtypes (mucinous adenocarcinoma, adenosquamous carcinoma) or malignant transformation of adenomas; tumor size less than 50 pixels on an axial plane of APTw imaging; and synchronous distant metastases.

Image acquisition

All patients underwent rectal MRI examinations in the supine position using a 3.0 T MRI scanner (INGENIA, Philips Healthcare, Best, The Netherlands) with a 16-channel phased-array coil. The imaging protocol included T1-weighted imaging (T1WI), high-resolution T2-weighted imaging (HR-T2WI), conventional DWI (b = 0, 1000 s/mm²), and APTw imaging. The 3D APTw imaging

parameters were as follows: repetition time (TR)/echo time (TE), 6306/10 ms; field of view, 230 × 180 × 60 mm; matrix, 128 × 100 × 6; slice thickness, 6 mm; spatial resolution, 1.8 × 1.8 × 6 mm^3; and TSE factor, 174. The complete MRI sequence parameters are summarized in Table 1.

Table 1 Main imaging parameters of the MRI protocol

Parameters	3D-APTw imaging	DWI	T2WI
Sequence	TSE	EPI	TSE
Repetition time/echo time (ms)	6306/8.3	2893/65	4562/100
Flip angle (degrees)	90	90	N/A
Field of view (mm^2)	230×180×60	260×260×140	260×260×140
Spatial Resolution (mm^3)	1.8×1.8×6	3×3×4	0.7×0.7×4
Matrix	128×100×6	88×86×4	372×324×4
Section thickness (mm)	6	4	4
TSE factor	174	N/A	25
b Values (s/mm^2)	N/A	0,1000	N/A
Fat suppression	SPIR	SPIR	N/A
Acquisition time (min:sec)	5:23	1:59	3:12

Image Quality Assessment

Two radiologists (Y.X.N. and J.Z., with 3 and 7 years of pelvic MRI experience, respectively) independently evaluated APTw image quality while being blinded to the pathological findings.

Assessment was performed using a validated four-point scale (Supplementary Table E1) based on established criteria. Representative examples of each quality score (1–4) are provided in Supplementary Figure E1. Any interobserver discrepancies were adjudicated by a senior radiologist (L.Z., with 10 years of pelvic MRI experience) to establish consensus.

Clinical-Radiological Data Collection and Follow-up

Clinical data (gender, age, carcinoembryonic antigen (CEA), carbohydrate antigen 19-9), and pathological characteristics (pTN stage, differentiation grade, perineural invasion, lymphovascular invasion) were extracted from electronic medical records. Radiological features, including MRI-based TNM staging, tumor-to-anal verge distance, and extramural vascular invasion (EMVI), were obtained from structured MR reports. Two blinded radiologists (Y.X.N. and J.Z.) independently evaluated all parameters. Consensus was achieved through joint review in cases of discrepant interpretations.

All patients underwent postoperative follow-up using abdominal ultrasound (US), contrast-enhanced computed tomography (CT), or MRI. Tumor recurrence or metastasis was defined based on typical imaging features observed on CT, MRI, or US, or on pathological results. Disease-free survival (DFS) was defined as the time from the date of surgery to the date of first recurrence, metastasis, or last follow-up. The follow-up period ended on June 1, 2025.

Tumor segmentation

Two radiologists (L.Z. and L.C.L., with 10 and 9 years of experience in pelvic MRI, respectively) performed the measurements using ITK-SNAP software (version 2.2.0; http://www.itksnap.org) and were blinded to the pathological results. First, the T2WI and DWI images were selected to identify the

tumor location and margin. Second, volumes of interest (VOIs) were manually delineated along the tumor margin on the ADC and S0 images. Third, the VOIs were then copied to the APTw and T2WI maps. Artifacts, blood vessels, regions of necrosis, and the tumor stalk were avoided.

Habitat generation

For tumor subregion segmentation, each tumor was first partitioned into 100 superpixels using the Simple Linear Iterative Clustering (SLIC) algorithm [23]. Subsequently, 19 first-order features were extracted from each superpixel. These features were then subjected to K-means clustering to identify distinct tumor habitats. To determine the optimal number of clusters, we evaluated a range of cluster counts (K) from 2 to 10 for each individual case. For each tested K value, the Calinski-Harabasz (CH) Index was computed for each individual case [24]. The CH-score was used to identify the case-wise optimal K value. After obtaining the original optimal K for each case, we calculated the frequency distribution of these K values across the entire cohort. The most-frequently-selected K values across the cohort were subsequently adopted as unified cluster numbers for respective sequences in downstream feature extraction.

Radiomics feature extraction and selection

A total of 1367 subregion radiomic features were independently extracted from the specified habitats and the whole-tumor region within APTw, DWI, and T2WI sequences, and were subsequently employed for further feature selection, respectively. For areas with insufficient voxel counts, a k-nearest neighbor approach was used to address missing data, thereby ensuring the robustness and reliability of the analysis. All features were extracted using PyRadiomics version 3.0.1

(http://pyradiomics.readthedocs.io) [25], following the guidelines of the Imaging Biomarker Standardization Initiative (IBSI) [26].

The distribution of features was normalized using the mean and standard deviation of this cohort. Statistical evaluation of features was performed using t-tests, with a significance threshold set at $P < 0.05$ to retain only statistically significant features. Highly correlated features were eliminated using Pearson's correlation, with the threshold set at 0.9. The least absolute shrinkage and selection operator (LASSO) regression was then applied to perform multifactor analysis for feature dimension reduction. The optimal regularization parameter λ was determined through 10-fold cross-validation to identify the most predictive features.

Model Development

The selected whole-tumor radiomics features were used to construct the radiomics signature, while habitat radiomics features were employed to establish the intratumoral heterogeneity (ITH) signature. The model development process was supervised; five classification algorithms implemented in R (version 4.5.1, https://www.r-project.org) were employed, including Logistic Regression (LR), Random Forest (RF), ExtraTrees, XGBoost, and LightGBM.

Based on the selected radiomic features, we constructed five models using habitat radiomics analysis: APTw, ADC, T2WI, APTw+ADC, and APTw+ADC+T2WI fusion sequence. Similarly, five radiomics predictive models (APTw, ADC, T2WI, APTw+ADC, and APTw+ADC+T2WI fusion sequence) and a clinical predictive model were constructed. Finally, the best predictive model was selected and combined with the selected clinical risk factors to construct a combined predictive model. The

complete analytical workflow is illustrated in Figure 1.

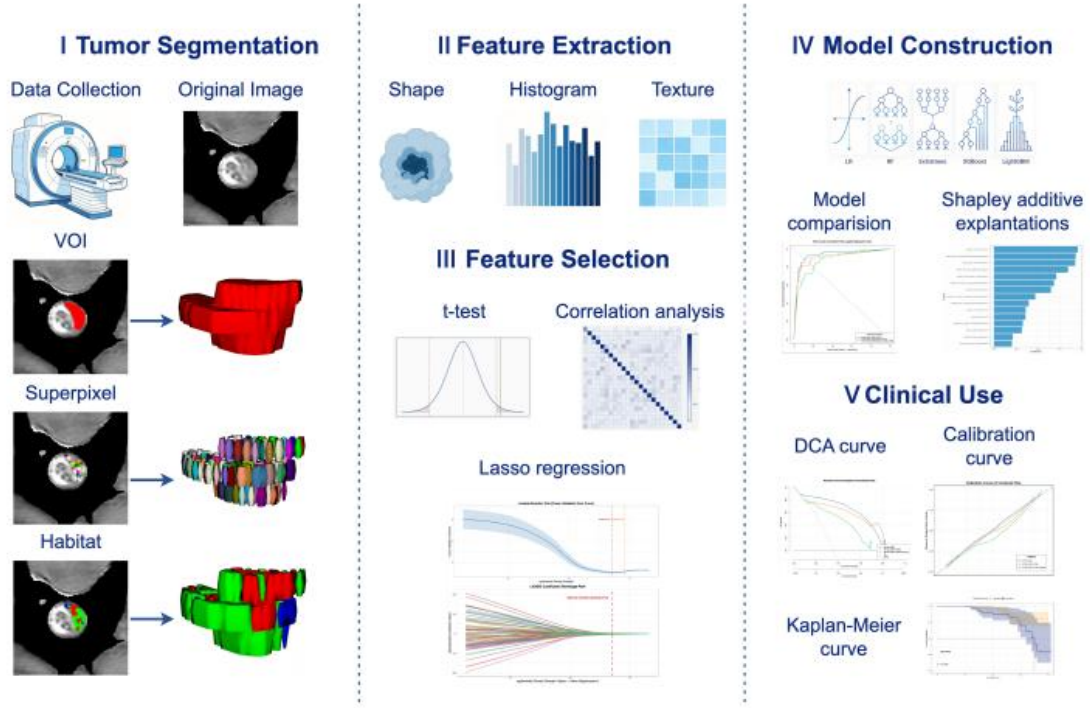


Figure 1 Flowchart of image analysis (By Figdraw)

Histopathology evaluation

According to the 2016 International Tumor Budding Consensus Conference (ITBCC) recommendations [7], surgical specimens were fixed, paraffin-embedded, sectioned, and stained with hematoxylin and eosin (H&E). Following slide mounting, two experienced pathologists (one with 5 years of diagnostic experience and one with 10 years of experience) independently evaluated the TB grade. Consensus was reached through joint review.

The assessment protocol comprised identification of the area with maximal TB density at low-power magnification and counting buds across 10 consecutive high-power fields within this hotspot. TB grades were classified using the Bud (Bd) scoring system: Bd1 (low grade), 0–4 buds/10 HPF; Bd2

(intermediate grade), 5–9 buds/10 HPF; Bd3 (high grade), ≥10 buds/10 HPF. Patients were stratified into two analytical groups based on pathological findings: the intermediate-to-low grade group (Bd1+2) and the high-grade group (Bd3).

Statistical analysis

The Kolmogorov–Smirnov test was used to assess the normality of quantitative variables. Normally distributed data were presented as mean ± standard deviation. Categorical variables were compared using the chi-square test or Fisher's exact test. Interobserver agreement for image quality was evaluated using Kappa (κ) statistics. Both inter- and intra-observer reproducibility of volume of interest (VOI) measurements were quantified using intraclass correlation coefficients (ICCs).

Receiver operating characteristic (ROC) curve analysis was used to evaluate the diagnostic performance of five habitat radiomics and five classical radiomics models (APTw, T2WI, ADC, APTw+ADC, APTw+ADC+T2WI), clinical models, and all combined models for distinguishing the low-intermediate TB grade Bd (1+2) group from the high TB grade (Bd 3) group. The AUCs and 95% confidence intervals (CIs) were calculated by K-fold cross-validation and compared via the DeLong method. Sensitivity and specificity metrics were calculated based on the optimal cutoff points derived from the ROC curves using the maximum Youden's index. The bootstrap test was used for internal validation. The calibration curve was used to evaluate the goodness of fit of the optimal model. Decision curve analysis was performed to compare the differences in net benefits between the different models at the threshold probability. Survival curves generated using the Kaplan-Meier method were

compared using the log-rank test. Statistical analysis was performed using R (version 4.5.1, https://www.r-project.org). $P < 0.05$ was considered statistically significant.

Results

Clinical characteristics

The study initially enrolled 418 participants. A total of 261 participants were excluded from the analysis for the following reasons: history of any antitumor therapy prior to MRI or surgery (n=122), presence of synchronous distant metastases (n=59), incomplete clinicopathological data (n=19), non-RA patients (n=59), and inadequate image quality for analysis (n=2). According to the above selection criteria, a total of 157 patients with RA were included in this study, including 90 males and 67 females, with an average age of 64.65 ± 11.29 years (range, 31–87 years). The flowchart of the participant selection process is presented in Figure 2.

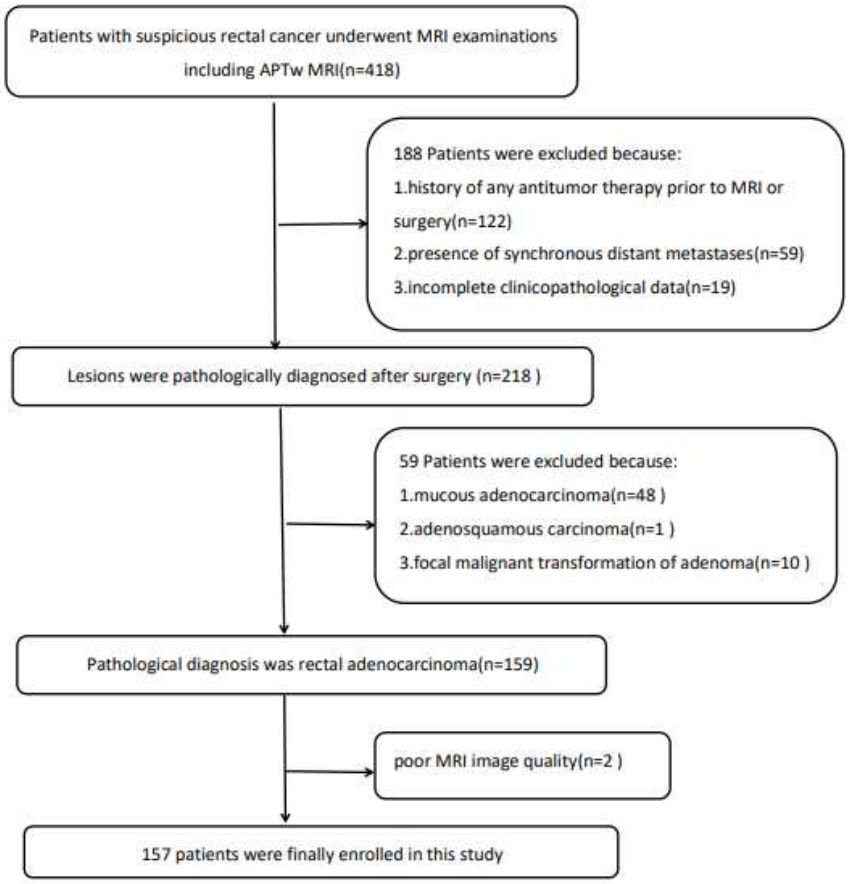


Figure 2 Flowchart of patient selection.

Additionally, only tumor differentiation, lymphovascular invasion, and perineural invasion were significantly different between the Bd 1+2 and Bd 3 groups (all $P < 0.05$). Table 2 summarizes the clinical characteristics of the patients in detail.

Table 2 Comparison of Clinical and imaging characteristics with different TB grade

Variable	TB grade		
	Bd 1+2 (n=102)	**Bd 3 (n=55)**	***P*-value**
Age	64.94 ± 10.49	64.04 ± 10.29	0.582

Sex			0.954
male	60 (58.82%)	30 (54.55%)	
female	42 (41.17%)	25 (45.45%)	
tumor location			0.337
lower	22 (21.57%)	11 (20.00%)	
middle	52 (50.98%)	25 (45.45%)	
upper	35 (34.31%)	19 (34.54%)	
MR T stage			0.129
T1-2	37 (36.27%)	15 (27.27%)	
T3-4	65 (63.73%)	40 (72.73%)	
MR N stage			0.265
N0	32 (31.37%)	14 (25.45%)	
N1-2	70 (68.62%)	41 (74.54%)	
MR EMVI			0.475
Negative	53 (51.96%)	31 (56.36%)	
Positive	49 (48.03%)	24 (43.64%)	
Differentiation			**0.042**
Well	7 (6.86%)	6 (10.90%)	
Moderate	91 (89.22%)	36 (65.45%)	
Poor	4 (3.92%)	13 (23.64%)	
Pathological T stage			0.323

T1-2	30 (29.41%)	26 (47.27%)	
T3-4	72 (70.59%)	29 (52.73%)	
Pathological N stage			0.465
N0	47 (46.08%)	32 (58.18%)	
N1-2	55 (53.92%)	23 (41.82%)	
Lymphovascular invasion			**0.046**
Negative	79 (77.45%)	32 (58.18%)	
Positive	23 (22.55%)	23 (41.82%)	
Perineural invasion			**0.034**
Negative	67 (65.67%)	15 (27.27%)	
Positive	35 (34.31%)	35 (63.64%)	
Tumor deposit			0.804
Negative	79 (77.45%)	44 (80.00%)	
Positive	23 (22.55%)	11 (20.00%)	
CEA(ng/mL) (%)			0.556
≥5	35 (34.31%)	23 (41.82%)	
<5	67 (65.69%)	32 (58.18%)	
CA199(u/mL) (%)			0.084
≥37	20 (19.61%)	14 (25.45%)	
<37	82 (80.39%)	41 (74.55%)	

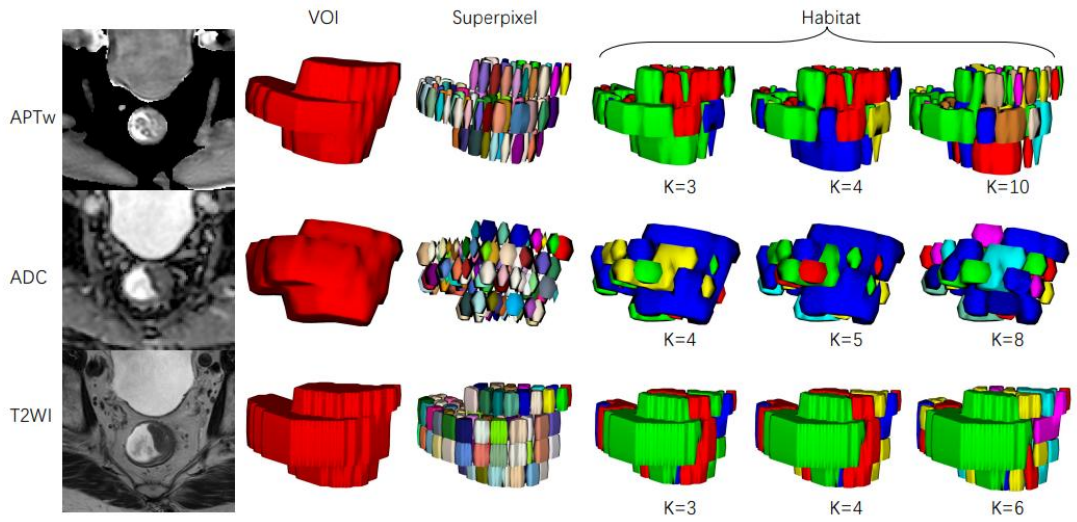
Image quality assessment

The participants (n=159) underwent APTw evaluation of image quality. The interobserver agreement for image quality scores was excellent for APTw ($\kappa = 0.84$; $P < 0.001$). There were 151 patients (151/159, 94.38%) with an APTw image quality score of 4. Two cases with image quality scores of 1–2 were excluded.

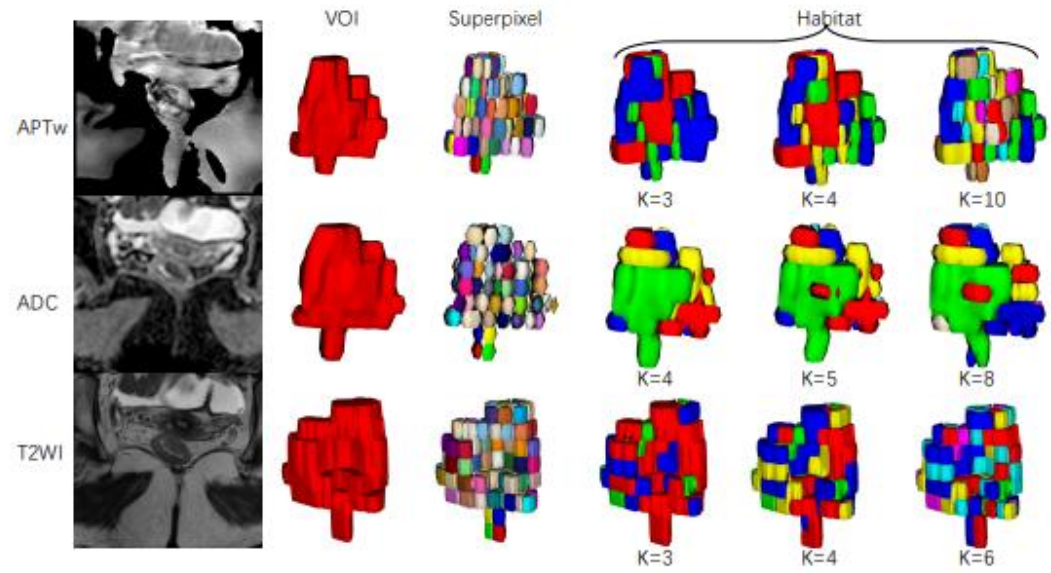
Feature extraction and selection

The ICC values of inter- and intraobserver reproducibility ranged from 0.853 to 0.927 for all measurements. All parameters derived from APTw demonstrated good reliability. The generation of habitat zones is visualized in Figure 3. The VOI of the tumor was segmented into 100 superpixels, which were subsequently clustered to delineate intratumoral habitat zones.

Optimal cluster numbers were determined as k=10 for APTw, k=8 for ADC, and k=4 for T2WI according to CH-score metrics. Each habitat subregion yielded 1367 radiomic features, leading to $k \times 1367$ candidate habitat-based radiomics features per MRI modality, where k denotes the optimized cluster number for each respective modality, for subsequent feature-selection analyses. After feature dimension reduction by Lasso, 26–60 of the most important habitat radiomics features were selected for the ITH signature. Figure 3 shows MRI scans in two patients whose TB grades were Bd 1 and Bd 3, respectively.



a



b

Figure 3 Example superpixel segmentation and habitat generation for patients with TB grades Bd 1 (a) and Bd 3 (b), respectively. Tumors are represented by different superpixels and habitats, indicated by different colors. The habitat zones were generated separately on APTw, ADC, and T2WI.

Model construction and performance

The LR classifier performed better than others in the establishment of the classification algorithm. ROC curves for both classical radiomics models and habitat-based radiomics models are presented in Figure 4. The diagnostic performance of various predictive models by K-fold cross-validation is shown in Table 3.

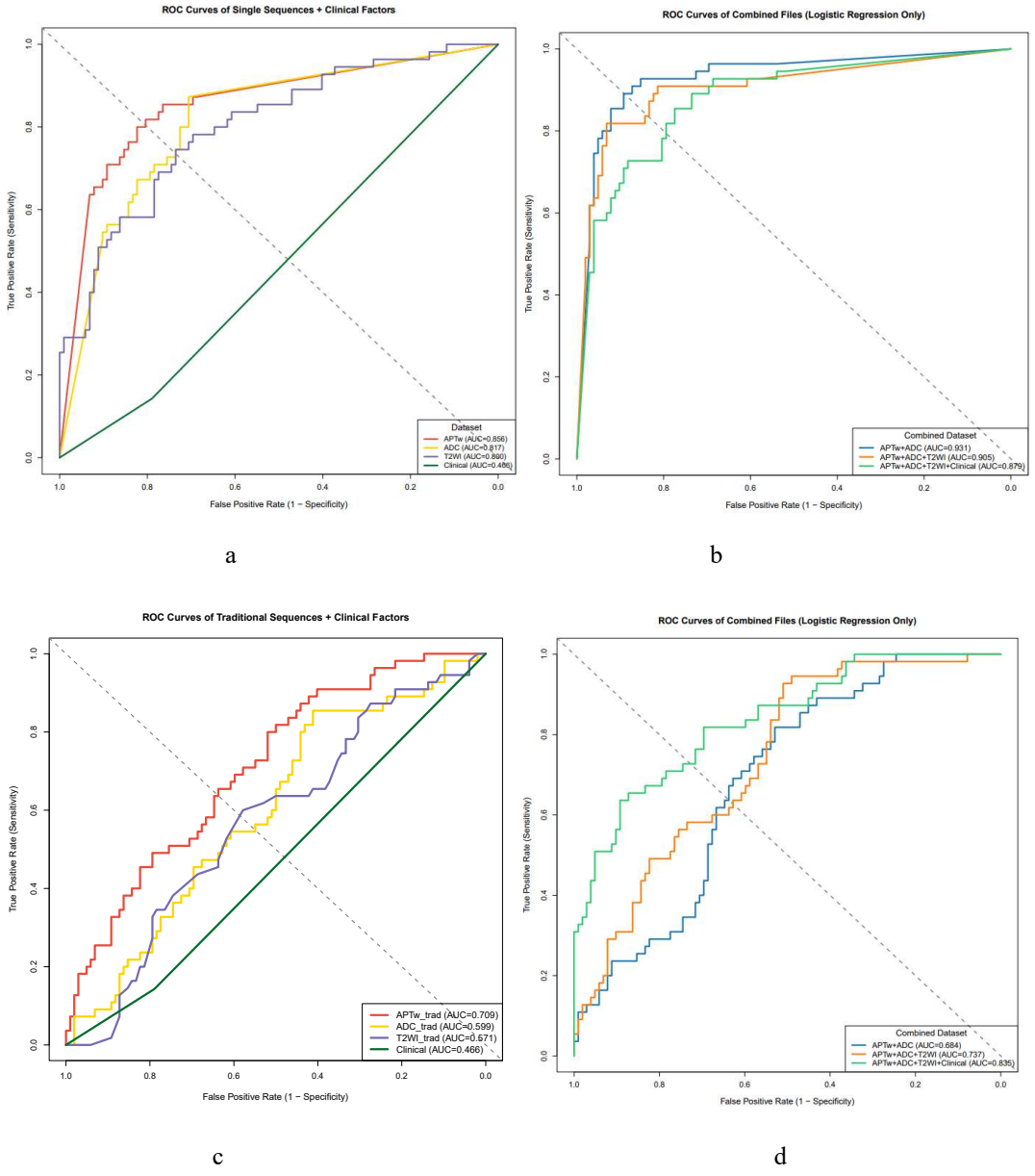


Figure 4 The ROC curves and corresponding AUCs of the classical and habitat radiomic models for discriminating Bd 3 from Bd 1+2 of rectal adenocarcinoma are shown. (a) represents the AUCs of habitat-based radiomics single models; (b) represents the AUCs of habitat-based radiomics combined

models; (c) represents the AUCs of classical radiomics single models; and (d) represents the AUCs of classical radiomics combined models.

In discriminating between Bd 1+2 and Bd 3, the AUC values of the APTw habitat-based radiomics model (at K=10) and the classical radiomics model were significantly higher than those of the T2WI and ADC models ($P < 0.05$). Furthermore, the combined model integrating both ADC and APTw features within the habitat-based radiomics framework achieved the best performance among all models, with an AUC of 0.931. DeLong's test showed no significant differences in AUC between the different habitat-based radiomics models ($P = 0.4113$ and 0.7922, respectively). However, the APTw+ADC model exhibited a higher lower confidence bound, PPV, and NPV compared to the other habitat-based models. Notably, the habitat-based radiomics models using APTw, ADC, and T2WI images each yielded significantly higher AUC values than their corresponding classical radiomics counterparts (all $P < 0.05$). The descriptions of the performance of each classifier and other diagnostic metrics are shown in Supplementary Tables E2 and E3.

Table 3 Diagnostic performance of different models for discriminating between Bd 1+2 and Bd 3 by K-fold cross-validation

Models	AUC(95%CI)	Sensitivity	Specificity	Accuracy	PPV	NPV
Classical Radiomics						
APTw	0.709(0.627,0.791)	0.8	0.52	0.618	0.473	0.828
ADC	0.599(0.508,0.69)	0.855	0.412	0.567	0.439	0.84
T2WI	0.539(0.442,0.636)	0.564	0.598	0.586	0.431	0.718

APTw+ADC	0.684(0.601,0.767)	0.818	0.529	0.631	0.484	0.844
APTw+ADC+T2WI	0.737(0.659,0.815)	0.927	0.51	0.656	0.505	0.929
APTw+ADC+T2WI+Clinical	0.835(0.77,0.9)	0.636	0.892	0.803	0.761	0.82
Habitat Radiomics						
APTw_10K	0.856(0.792,0.919)	0.824	0.815	0.71	0.884	0.884
ADC_8K	0.817(0.75,0.884)	0.706	0.764	0.615	0.911	0.911
T2WI_4K	0.768(0.693,0.843)	0.676	0.707	0.56	0.841	0.841
Clinical	0.466(0.407,0.609)	0.235	0.389	0.322	0.571	0.571
APTw+ADC	0.931(0.886,0.977)	0.892	0.892	0.817	0.938	0.938
APTw+ADC+T2WI	0.905(0.85,0.96)	0.931	0.892	0.865	0.905	0.905
APTw+ADC+T2WI+Clinical	0.879(0.821,0.936)	0.775	0.803	0.671	0.908	0.908

Clinicoradiological model

Univariate analysis revealed a significant association between tumour differentiation and Bd 3 status. After multivariate analysis, only tumour differentiation remained independently associated with high-grade TB (Bd 3 vs. Bd 1+2; odds ratio [OR] = 2.82 (1.29-6.19), P = 0.010) (Table 4). The AUC of the clinicoradiological model for discriminating Bd 3 from Bd 1+2 was 0.466, indicating that this clinical-only combination exhibited no meaningful discriminative capacity for stratifying TB grade.

Table 4 Results of univariate and multivariate logistic regression analyses to distinguish Bd (1+2) from Bd 3

Variables	Univariate logistic regression	Multivariate logistic regression

	OR (95%CI)	*P* values	OR (95%CI)	*P* values
Age	1.00 (0.97-1.03)	0.959	NA	NA
Gender	0.81 (0.42-1.56)	0.525	NA	NA
CA199	1.87 (0.77-4.58)	0.168	NA	NA
CEA	1.74 (0.89-3.42)	0.106	NA	NA
MR T	1.03 (0.51-2.06)	0.939	NA	NA
MR N	1.02 (0.49-2.09)	0.966	NA	NA
EMVI	0.98 (0.50-1.88)	0.94	NA	NA
Tumor Differentiation	2.82 (1.29-6.19)	0.01 [a]	2.82 (1.29-6.19)	0.01 [a]
Tumor Location	1.41 (0.30-6.56)	0.658	NA	NA
Pathology T	1.16 (0.56-2.41)	0.682	NA	NA
Pathology N	1.02 (0.53-1.98)	0.952	NA	NA
Nerve Invasion	1.44 (0.74-2.80)	0.052	NA	NA
Lymph Invasion	1.47 (0.72-2.98)	0.051	NA	NA

[a] $P < 0.05$.

CEA: Carcinoembryonic antigen; CA19-9: Carbohydrate antigen 19-9; EMVI: MRI-based extramural vascular invasion; OR: Odds ratio; CI: Confidence interval; NA: Not available.

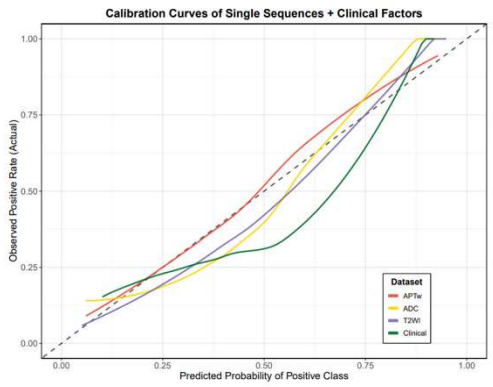
Internal validation

The bootstrap test was used for internal validation. In discriminating between Bd 1+2 and Bd 3, the habitat-based radiomics model (APTw+ADC) achieved an AUC of 0.931 (0.886, 0.977) in the internal

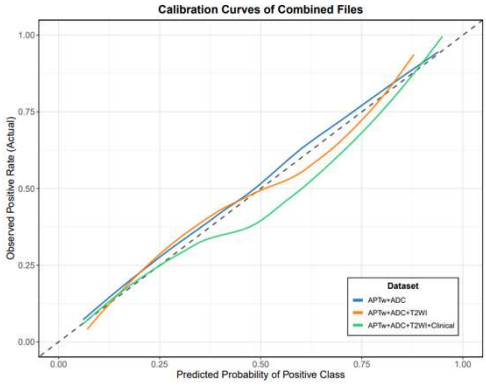
validation cohort, with sensitivity of 89%, specificity of 89%, accuracy of 82%, and a kappa value of 0.50, respectively. The description of the performance of each predictive model is shown in Supplementary Table E4.

Model evaluation

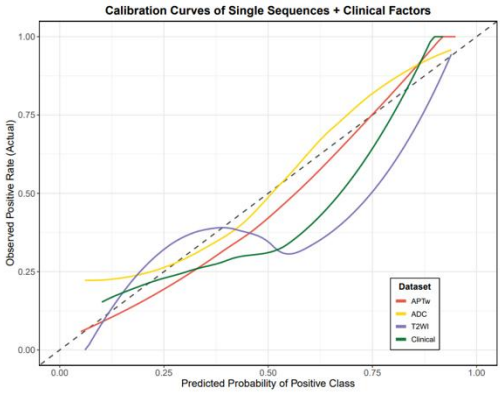
The calibration curves demonstrated consistency between the predicted and observed outcomes of Bd3. The calibration curves of APTw, ADC, T2WI, and the integrated model were all close to the gray line, with Hosmer–Lemeshow test values of $P = 0.0503–0.795$ (all $P > 0.05$), indicating good calibration. The calibration curves are presented in Figure 5.



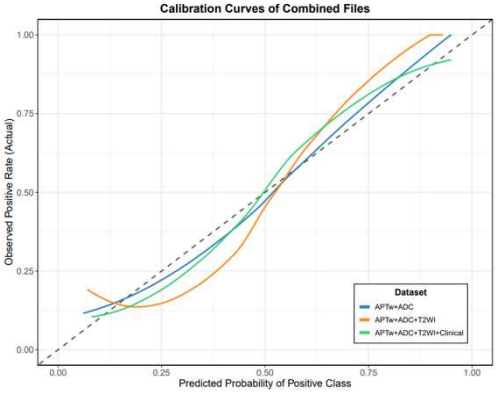
a



b



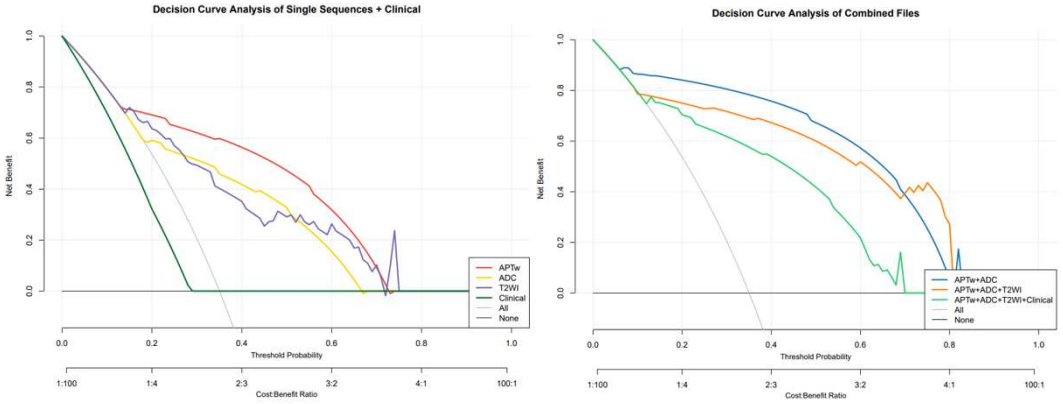
c



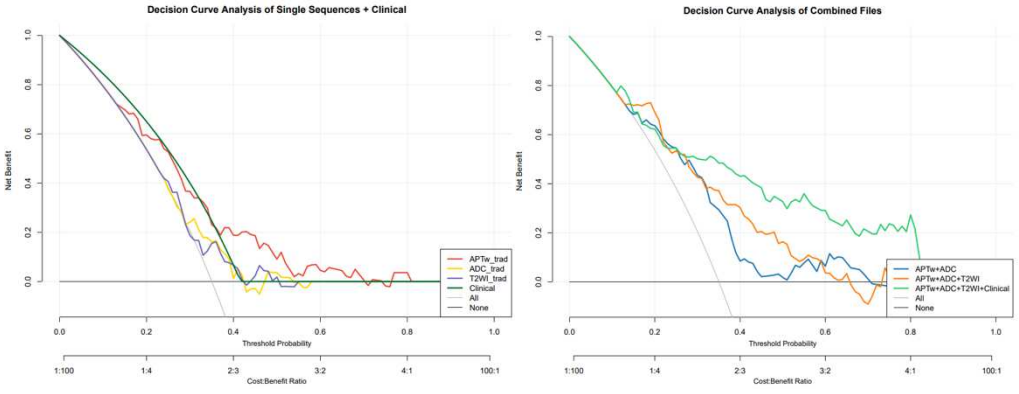
d

Figure 5 Calibration curves (a) The calibration curves of the habitat-based radiomics single models; (b) The calibration curves of the habitat-based radiomics of the combined models; (c) The calibration curves of classical radiomics single models; (d) The calibration curves of classical radiomics combined models

The DCAs of APTw, ADC, T2WI, and the integrated model are presented in Figure 6. The net benefit yielded by the APTw+ADC habitat-based radiomics model was slightly higher compared with other combined models. The decision curve showed that if the threshold probability was between 0.1 and 0.7, then using the APTw+ADC habitat model to assess Bd 3 provided more benefit than treating either all patients or none.



a b

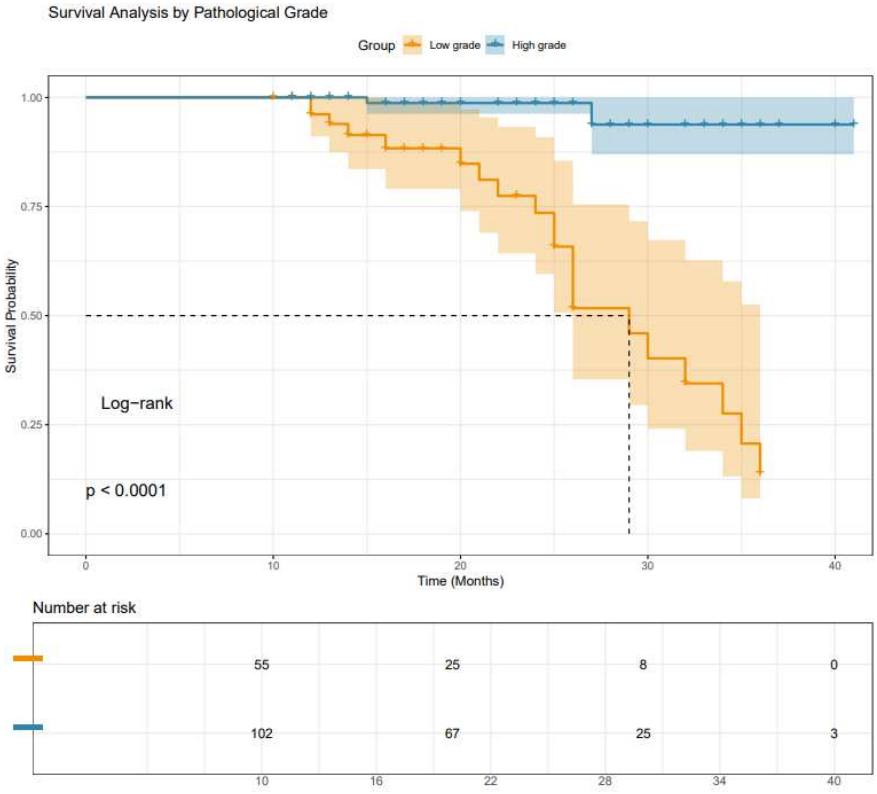


c d

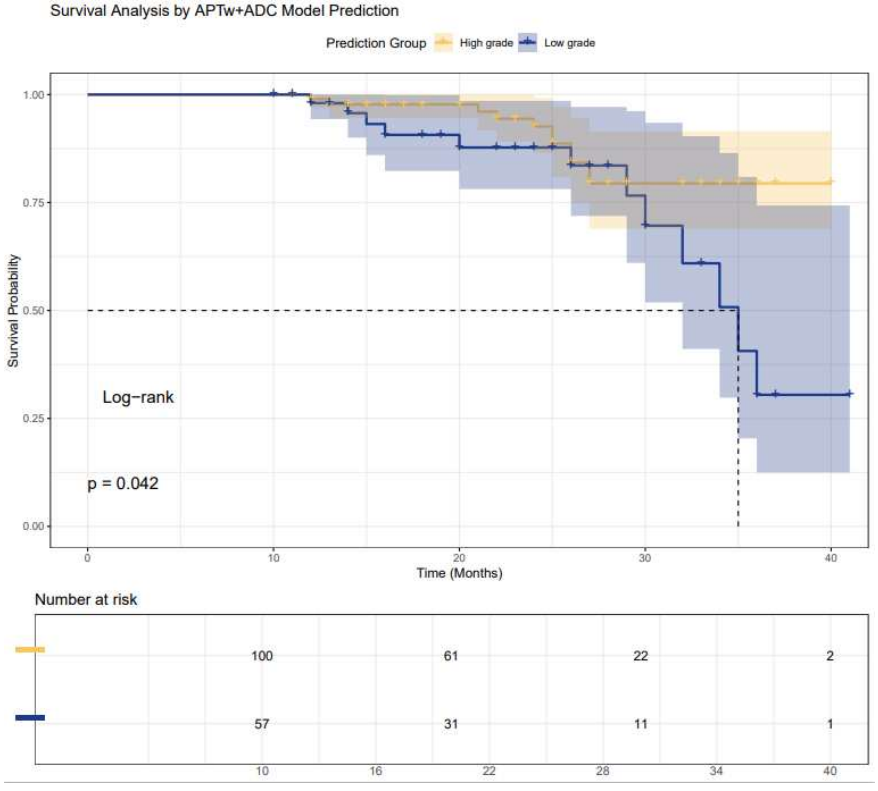
Figure 6 Decision curves(a) Decision curve analysis of the habitat-based radiomics single models; (b) Decision curve analysis of the habitat-based radiomics of the combined models; (c) Decision curve analysis of the classical radiomics single models; (d) Decision curve analysis of the classical radiomics combined models

Prognostic analysis of the optimal model

Follow-up data were available for 157 patients. The median follow-up period for the entire cohort was 25 months (range: 10–48). The Bd 3 group exhibited a significantly worse 2-year DFS rate compared to the Bd 1+2 group (58.8% vs. 94.17%, P=0.022). Kaplan–Meier analysis further demonstrated that patients stratified into the Bd 3 group by the APTw+ADC habitat-based radiomics model had significantly worse DFS than those in the Bd 1+2 group (P<0.05) (Figure 7). Univariate and multivariate Cox proportional hazards analyses identified this model as a significant risk factor for 2-year DFS (hazard ratio [HR]=1.26, 95% CI: 1.05–1.93, P=0.042).


Survival Analysis by Pathological Grade
Group
Low grade
High grade
Survival Probability
1.00
0.75
0.50
0.25
0.00
Log−rank
p < 0.0001
0
10
20
30
40
Time (Months)
Number at risk
55
25
8
0
102
67
25
3
10
16
22
28
34
40

a


Survival Analysis by APTw+ADC Model Prediction
Prediction Group
High grade
Low grade
Survival Probability
1.00
0.75
0.50
0.25
0.00
Log−rank
p = 0.042
0
10
20
30
40
Time (Months)
Number at risk
100
61
22
2
57
31
11
1
10
16
22
28
34
40

b

Figure 7 Kaplan-Meier survival curves according to pathological TB grade (a) and Bd 3 predicted by the APTw+ADC habitat-based radiomics model in the whole cohort (b).

Discussion

Precise preoperative risk stratification and prognostic profiling constitute critical unmet clinical needs for patients with rectal adenocarcinoma. Conventional whole-tumor radiomics methodologies conceptualize the neoplastic lesion as a biologically homogeneous entity and largely disregard intratumoral heterogeneity, thereby constraining their performance in characterizing aggressive pathological phenotypes such as high-grade tumor budding [12,21]. Against this backdrop, the primary novelty of the present work resides in the implementation of habitat-driven subregional segmentation, which enables deconvolution of biologically distinct intratumoral compartments beyond the analytical scope of conventional whole-tumor frameworks [18,27]. By integrating protein-metabolic heterogeneity derived from APTw imaging and microstructural alterations reflected by ADC maps, this multiparametric habitat radiomics paradigm captures two complementary biological dimensions of rectal malignancy, representing a feasible strategy for dissecting complex tumour microenvironment features [28]. Beyond differentiating pathological tumor-budding grades, the constructed imaging signature confers additional prognostic utility for postoperative disease-free survival, underscoring that combined subregional metabolic-structural features can substantially inform preoperative risk stratification to facilitate clinical decision-making.

Existing predictive investigations addressing tumor-budding status in rectal adenocarcinoma predominantly rely on clinical covariates, routine morphological MRI sequences, or conventional whole-tumor radiomics workflows [14-17]. Many existing radiomics efforts in rectal cancer are oriented toward neoadjuvant treatment-response prediction rather than tumour-budding-related risk stratification [29]. To our knowledge, few prior studies have integrated APTw molecular metabolic MRI with habitat-based subregion analysis for preoperative TB-grade risk assessment in rectal adenocarcinoma; furthermore, most radiomics-driven predictive efforts terminate at pathological classification without subsequent validation of prognostic performance. The improved performance afforded by our habitat-centered pipeline may be partially attributed to the capacity of APTw-derived metabolic heterogeneity to recapitulate the intrinsic biological behaviours associated with tumour invasion and tumour budding. Conventional whole-tumor radiomics averages imaging signals across the entire tumour volume, which risks diluting discriminative signals originating from spatially confined yet highly aggressive sub-compartments. In contrast, habitat-based analytics preserve spatially resolved subregional tumour information, yielding incremental pathological and prognostic insights that are inaccessible to conventional prediction modalities [19].

Mechanistically, high-grade tumour budding represents a pathological readout of augmented invasive and migratory potential, which is intimately coupled to epithelial-mesenchymal transition programmes [6]. Patients harbouring high-grade TB exhibit elevated postoperative recurrence risk and dismal long-term oncological outcomes, highlighting the clinical imperative to non-invasively identify this high-risk subgroup preoperatively. APTw MRI quantifies mobile intracellular amide-proton signals reflecting tumour proliferative activity and protein biosynthesis; this signal is also modulated by the

local tissue pH microenvironment [30], whereas ADC metrics characterise tumour cellular density and parenchymal microstructural disarray [20,31]. Malignant lesions are biologically non-uniform; heterogeneous subregions demarcated via habitat segmentation correspond to high-risk tumour compartments enriched for invasive neoplastic clones. Accordingly, joint interrogation of metabolic and structural signatures originating from these subregions affords superior biological interpretability for identifying high-grade TB and stratifying recurrence-associated patient subgroups, relative to global whole-tumour-based assessments.

Several inherent limitations of this study should be acknowledged. First, all imaging datasets were acquired at a single tertiary institution using standardized MRI hardware, and no independent external cohort was available to corroborate the generalizability of the established predictive signature. Second, despite acceptable sample size for single-centre radiomics research, the present cohort remains moderately sized. Future large-scale multicentre prospective cohorts are warranted to rigorously validate both the predictive robustness and real-world prognostic-stratification performance of this habitat-based strategy. Notwithstanding these constraints, our multiparametric habitat radiomics framework demonstrates tangible conceptual and analytical advantages over conventional prediction approaches, establishing a linkage between preoperative subregional multiparametric MRI features and both pathological tumour-budding status and postoperative oncological endpoints. In summary, the APTw-plus-ADC habitat radiomics model can serve as a non-invasive preoperative risk-stratification tool for patients with rectal adenocarcinoma.

Data Availability Statement

The datasets generated and/or analysed during the current study are available from the corresponding author on reasonable request.

Declarations

Abbreviations

ADC	Apparent diffusion coefficient
APTw	Amide proton transfer-weighted
AUC	Area under the curve
CRC	Colorectal cancer
DCA	Decision curve analysis
DFS	Disease-free survival
DWI	Diffusion-weighted imaging
EMVI	Extramural vascular invasion
LASSO	Least absolute shrinkage and selection operator
RA	Rectal adenocarcinoma
ROC	Receiver operating characteristic
T2WI	T2-weighted imaging
TB	Tumour budding
TNM	Tumour–node–metastasis
VOIs	Volumes of interest

Ethics approval and consent to participate

This prospective study was approved by the Ethics Committee of Shaanxi Provincial People's Hospital (approval number: 2022K-133). All procedures were performed in accordance with the principles of the Declaration of Helsinki. Written informed consent was obtained from all enrolled patients before MRI examination.

Consent for publication

Not applicable

Availability of data and materials

The datasets generated and/or analysed during the current study are available from the corresponding author on reasonable request.

Competing interests

The authors declare that they have no competing interests.

Funding

This work was supported by the Science and Technology Talent Support Plan of Shaanxi Provincial People's Hospital (Grant No: 2023JY-29), awarded to Jing Zhang.

Authors' contributions

JZ: Funding Acquisition, Software, Writing – Original Draft, Writing – Review & Editing.

LL: Conceptualization, Formal Analysis, Data Curation, Writing – Original Draft.

MT: Conceptualization, Formal Analysis, Writing – Original Draft.

XL: Conceptualization, Data Curation, Software, Writing – Original Draft.

LZ: Data Curation, Supervision, Validation, Writing – Review & Editing.

XD: Supervision, Validation, Visualization, Writing – Review & Editing.

Acknowledgements

None

References

1. Siegel R L, Giaquinto A N, Jemal A. Cancer statistics, 2024. CA Cancer J Clin. 2024;74:12-49. doi:10.3322/caac.21820.

2. Deng Y. Rectal Cancer in Asian vs. Western Countries: Why the Variation in Incidence? Curr Treat Options Oncol. 2017;18:64. doi:10.1007/s11864-017-0505-2.

3. Benson A B, Venook A P, Al-Hawary M M, et al. Rectal Cancer, Version 2.2022, NCCN Clinical Practice Guidelines in Oncology. J Natl Compr Canc Netw. 2022;20:1139-1167. doi:10.6004/jnccn.2022.0053.

4. Weiser M R. AJCC 8th Edition: Colorectal Cancer. Ann Surg Oncol. 2018;25:1454-1455. doi:10.1245/s10434-018-6462-5.

5. Dienstmann R, Vermeulen L, Guinney J, et al. Consensus molecular subtypes and the evolution of precision medicine in colorectal cancer. Nat Rev Cancer. 2017;17:79-92. doi:10.1038/nrc.2016.126.

6. Lugli A, Zlobec I, Berger M D, Kirsch R, Nagtegaal I D. Tumour budding in solid cancers. Nat Rev Clin Oncol. 2021;18:101-115. doi:10.1038/s41571-020-00422-y.

7. Lugli A, Kirsch R, Ajioka Y, et al. Recommendations for reporting tumor budding in colorectal cancer based on the International Tumor Budding Consensus Conference (ITBCC) 2016. Mod Pathol. 2017;30:1299-1311. doi:10.1038/modpathol.2017.46.

8. Saito K, Okuyama T, Miyazaki S, et al. Tumor Budding as a Predictive Marker of Relapse and Survival in Patients With Stage II Colon Cancer. In Vivo. 2022;36:1820-1828. doi:10.21873/invivo.12879.

9. Rogers A C, Gibbons D, Hanly A M, et al. Prognostic significance of tumor budding in rectal cancer biopsies before neoadjuvant therapy. Mod Pathol. 2014;27:156-162. doi:10.1038/modpathol.2013.125.

10. Trotsyuk I, Sparschuh H, Müller A J, et al. Tumor budding outperforms ypT and ypN classification in predicting outcome of rectal cancer after neoadjuvant chemoradiotherapy. BMC Cancer. 2019;19:1033. doi:10.1186/s12885-019-6241-8.

11. Jäger T, Neureiter D, Fallaha M, et al. The potential predictive value of tumor budding for neoadjuvant chemoradiotherapy response in locally advanced rectal cancer. Strahlenther Onkol. 2018;194:991-1006. doi:10.1007/s00066-018-1307-1.

12. Marusyk A, Almendro V, Polyak K. Intra-tumour heterogeneity: a looking-glass for cancer? Nat Rev Cancer. 2012;12:323-334. doi:10.1038/nrc3236.

13. Zengin M, Çifci A. Tumour budding in preoperative biopsy specimens is a useful prognostic index for identifying high-risk patients in early-stage (pN0) colon cancer. Turk J Med Sci. 2020;50:375-385. doi:10.3906/sag-1905-184.

14. Qu X, Zhang L, Ji W, Lin J, Wang G. Preoperative prediction of tumor budding in rectal cancer using multiple machine learning algorithms based on MRI T2WI radiomics. Front Oncol. 2023;13:1267838. doi:10.3389/fonc.2023.1267838.

15. Peng L, Wang D, Zhuang Z, et al. Preoperative Noninvasive Evaluation of Tumor Budding in Rectal Cancer Using Multiparameter MRI Radiomics. Acad Radiol. 2024;31:2334-2345. doi:10.1016/j.acra.2024.01.012.

16. Liu Z, Jia J, Bai F, et al. Predicting rectal cancer tumor budding grading based on MRI and CT with multimodal deep transfer learning: A dual-center study. Heliyon. 2024;10:e28769. doi:10.1016/j.heliyon.2024.e28769.

17. Jia J, Kang Y, Wang J, et al. Attention mechanism-based multi-parametric MRI ensemble model for predicting tumor budding grade in rectal cancer patients. Abdom Radiol (NY). 2025;50:4483-4494. doi:10.1007/s00261-024-04611-4.

18. Tolkach Y, Kristiansen G. The Heterogeneity of Prostate Cancer: A Practical Approach. Pathobiology. 2018;85:108-116. doi:10.1159/000486412.

19. Tomaszewski M R, Gillies R J. The Biological Meaning of Radiomic Features. Radiology. 2021;298:505-516. doi:10.1148/radiol.2021201933.

20. Kamimura K, Nakajo M, Yoneyama T, et al. Amide proton transfer imaging of tumors: theory, clinical applications, pitfalls, and future directions. Jpn J Radiol. 2019;37:109-116. doi:10.1007/s11604-018-0711-1.

21. Xie P, Huang Q, Zheng L, et al. Sub-region based histogram analysis of amide proton transfer-weighted MRI for predicting tumor budding grade in rectal adenocarcinoma: a prospective study. Eur Radiol. 2025;35:1382-1393. doi:10.1007/s00330-024-13208-8.

22. Wang H J, Cai Q, Huang Y P, et al. Amide Proton Transfer-weighted MRI in Predicting Histologic Grade of Bladder Cancer. Radiology. 2022;305(1):127-134. doi:10.1148/radiol.212635.

23. Achanta R, Shaji A, Smith K, et al. SLIC superpixels compared to state-of-the-art superpixel methods. IEEE Trans Pattern Anal Mach Intell. 2012;34:2274-2282. doi:10.1109/TPAMI.2012.120.

24. Liu Y, Li Z, Xiong H, et al. Understanding and enhancement of internal clustering validation measures. IEEE Trans Cybern. 2013;43:982-994. doi:10.1109/TCYB.2012.2205661.

25. van Griethuysen J J M, Fedorov A, Parmar C, et al. Computational Radiomics System to Decode the Radiographic Phenotype. Cancer Res. 2017;77:e104-e107. doi:10.1158/0008-5472.CAN-17-0339.

26. Zwanenburg A, Vallières M, Abdalah M A, et al. The Image Biomarker Standardization Initiative: Standardized Quantitative Radiomics for High-Throughput Image-based Phenotyping. Radiology. 2020;295:328-338. doi:10.1148/radiol.2019191847.

27. Cai Z, Xu Z, Chen Y, et al. Multiparametric MRI subregion radiomics for preoperative assessment of high-risk subregions in microsatellite instability of rectal cancer patients: a multicenter study. Int J Surg. 2024;110:4310-4319. doi:10.1016/j.ijsu.2024.06.016.

28. Matsumoto K I, Mitchell J B, Krishna M C. Multimodal Functional Imaging for Cancer/Tumor Microenvironments Based on MRI, EPRI, and PET. Molecules. 2021;26:1614. doi:10.3390/molecules26061614.

29. Bourbonne V, Schick U, Pradier O, et al. Radiomics Approaches for the Prediction of Pathological Complete Response after Neoadjuvant Treatment in Locally Advanced Rectal Cancer: Ready for Prime Time? Cancers (Basel). 2023;15:432. doi:10.3390/cancers15020432.

30. Zhou J, Payen J F, Wilson D A, et al. Using the amide proton signals of intracellular proteins and peptides to detect pH effects in MRI. Nat Med. 2003;9:1085-1090. doi:10.1038/nm907.

31. Zhou J, Heo H Y, Knutsson L, van Zijl P C M, Jiang S. APT-weighted MRI: Techniques, current neuro applications, and challenging issues. J Magn Reson Imaging. 2019;50:347-364. doi:10.1002/jmri.26645.

Supplementary Files

This is a list of supplementary files associated with this preprint. Click to download.

- SUPPLEMENTARYMATERIAL.docx